Surface & Coatings Technology 481 (2024) 130614

Contents lists available at ScienceDirect

Surface & Coatings Technology

journal homepage: www.elsevier.com/locate/surfcoat

Full Length Article

Effect of substrate microstructure on corrosion resistance of cast and forged anodised 6082 Al alloy

B. Díaz [a], R. Figueroa [a,*], X.R. Nóvoa [a], C. Pérez [a,*], S. Pérez-Betanzos [b], S. Valverde-Pérez [a]

[a] CINTECX, Universidade de Vigo, ENCOMAT Group, E.E.I. Campus Universitario, 36310 Vigo, Spain
[b] CIE Galfor (CIE Automotive Group), P.I. San Cibrao das Viñas, 32901 Ourense, Spain

ARTICLE INFO

Keywords:
6082 aluminium alloy
Billets
Anodised layer
Forgings
Corrosion resistance

ABSTRACT

This work addresses the effect of the surface morphology of a 6082-aluminium alloy on the characteristics of the anodic layer generated by an anodising process using two current densities. The samples tested were horizontal direct chill (HDC), vertical direct chill (VDC) cast billets, and the same material after forged + T6 ageing treatment. Samples were anodised in a mixed citric acid-sulphuric acid electrolyte using 0.5 $A{\cdot}dm^{-2}$ and 1.5 $A{\cdot}dm^{-2}$. D.C. current densities. The protective character of the oxide layer was studied by electrochemical impedance spectroscopy (EIS) in 0.1 M NaCl solution.

Microstructural characterisation revealed that the microsegregation and forging processes have a significant effect on the growth of the oxide layer as well as on the optimum anodising conditions. The EIS study showed that the corrosion protection provided by the oxide layer on Al6082 alloy was strongly affected by the manufacturing process, with thinner oxide layers obtained for cast billets. Heat treatment and forging homogenise the microstructure, which positively affects anodising and modifies the growth rate and thickness of the oxide layer. This effect makes obtaining a thicker oxide layer with good corrosion protective properties possible by using lower current densities for forged samples.

1. Introduction

Aluminium and its alloys are characterised by the spontaneous generation of a native oxide under atmospheric conditions which provides inherent corrosion resistance. However, the reduced thickness and non-uniform structure of this layer do not provide adequate protection, especially in high-strength alloys. The alloying elements used to strengthen the aluminium matrix produce second phases in the microstructure with different electrochemical potentials [1], which can lead to galvanic coupling and the corrosion of the aluminium matrix in the presence of electrolyte and specially in aggressive media with chlorides or sulphates [1–3]. Therefore, it is necessary to apply different types of surface treatments to improve the corrosion behaviour of aluminium alloys. One of the most widespread processes is anodising [1,4], which generates a hard layer on the surface that provides good corrosion and wear resistance. Additionally, anodising can be combined with other treatments, such as incorporating corrosion inhibitors and organic coatings [5,6].

The anodising process involves the electrolytic growth of an anodic aluminium oxide (AAO) layer. Its properties depend on the anodising process, particularly on the nature and concentration of the electrolyte and on electrochemical parameters such as temperature, time, voltage and current [4,7,8]. From a corrosion resistance point of view, traditionally, using anodising and chemical conversion coatings was based on hexavalent chromium, as it provides effective corrosion protection, combining good coating adhesion and fatigue resistance [9–11]. However, the inherent toxicity of these species has restricted their use, and in the future they will be banned altogether [1]. The alternatives are based on acid electrolytes, the most commonly used being sulphuric acid, oxalic acid and phosphoric acid [12]. However, these media generate too brittle layers with low porosity that do not allow adequate adhesion of the coatings. The use of mixed electrolytes that combine an inorganic acid, usually sulphuric acid, and a weak organic acid, such as oxalic, malic, tartaric or citric acid, reduces these drawbacks and offers specific improvements in AAO properties [13]. These are attributed to the presence of fewer defects in the layer, the delay in the growth of stable pits [1], and the formation of complex species with Al^{3+} that slow the oxidation process [14]. The role of anions of different nature in the morphology of the anodic layers still under study [15]. The AAO layer in these acidic media consists of a thin, compact oxide layer (barrier layer)

* Corresponding authors.
E-mail addresses: raulfm@uvigo.gal (R. Figueroa), cperez@uvigo.gal (C. Pérez).

https://doi.org/10.1016/j.surfcoat.2024.130614
Received 30 December 2023; Received in revised form 14 February 2024; Accepted 29 February 2024
Available online 8 March 2024

on the aluminium substrate and a thicker porous film extending from the compact region to the surface [12,16]. The porosity of the oxide layer is highly dependent on the type of aluminium alloy, showing pores perpendicular to the surface for unalloyed and low-alloy aluminium. The columnar structure and continuity of the layer can be modified due to the presence of alloying elements. For example, the presence of Cu produces an irregular pattern and lateral porosity [17,18]. In addition, alloying elements such as Fe, Mn, Si and Mg, which form intermetallic particles, generate important changes in the AAO [19] and the appearance of defects that can inhibit the growth of the layer [16,20]. The type of defect generated depends largely on the corrosion rate of these particles in the electrolytic medium with respect to the matrix. Particles with anodic behaviour easily oxidise or dissolve in the medium and cause voids in the oxide layer. In contrast, particles that are electrochemically more noble than the aluminium matrix promote the oxidation of the surrounding matrix, and can generate voids due to the occlusion of oxygen generated on their surface during anodising [21,22] and even partially prevent the oxidation of the matrix by retaining non-anodised areas inside the oxide layer [23].

Numerous studies deal with the corrosion resistance of Al alloys after anodising. However, most of them focus on the high-strength Al alloys of the 2xxx, 6xxx and 7xxx series due to the high demand from the aerospace industry [13,20,22,24–27]. The 6082 aluminium alloy is an age-hardening alloy of the Al-Mg-Si system widely used in the automotive industry as it combines high specific strength and good formability [28–30]. The heat treatment process affects its mechanical properties and corrosion resistance, so most research has focused on optimising these heat treatments [31–33]. Fewer studies can be found on the anodising process of this alloy [8,34]. An additional aspect that has not been addressed in detail is the effect of the surface condition of the material before the anodising process in the anodic layer generated and, mainly its corrosion resistance. Caliari et al. [35] studied the influence of machining processes, such as milling or sandblasting operations, before anodising the Al-Si-Cu alloy. They concluded that these operations lead to an increase in the anodic layer. However, the corrosion resistance of the anodised samples was not characterised. Birol et al. [36] reported that forging produces a more uniform grain structure and superior surface quality than the castings. Only a microstructural study was performed, and the pieces were not anodised. Shan et al. [37] demonstrate the better corrosion resistance of forged samples compared to extruded ones using polarisation experiments, but samples were not anodised.

Therefore, the present work is focused on the comparative study of the anodised 6082 aluminium alloy from two states: as-cast billets and after forging. The billets were obtained from two technologies: horizontal direct chill (HDC) and vertical direct chill (VDC) casting. The samples were provided by a factory in the automotive sector (CIE Galfor) and are the same that they use in its activity. This aspect is new. Most of the studies in AA alloys used non-finished pieces. Microstructural characterisation was performed before anodising, both in billets and forgings. The electrochemical study was carried out after anodising.

2. Experimental design

2.1. Materials

The present study has been carried out on industrial-scale casting AA 6082 aluminium alloys. The formats supplied were billets obtained by horizontal direct chill (HDC) casting and vertical direct chill (VDC) casting. Details of these technologies can be found in [38]. The composition of the alloys is displayed in Table 1, together with the nominal composition according to EN 573-3 standard [39].

The CIE Galfor® (Automotive Group) performed the forging process from the billets supplied. The billets were preheated to 450 °C and forged on a 1600 t forging press. The forged pieces were subjected to a T6 age hardening treatment by solubilising at 530 °C for 2 h, quenched in water, and artificially aged at 180 °C for 8 h [40].

Before anodising, samples with dimensions 50mmx20mmx4mm were grounded with SiC grit papers up to 1200 grade; then, they were degreased in acetone, rinsed in deionised water, and dried in a cold air stream. Afterwards, they were alkaline etched in a 1 M NaOH solution for 3 min at 40 °C following by immersion in 1 M HNO_3 for 30 s at room temperature to remove the smut. Finally, they were rinsed thoroughly in deionised water.

Anodising was done using a mixed electrolyte, combining 2 M citric acid and 1 % vol. sulphuric acid. The electrolyte was kept at a low temperature, 5 °C, to reduce the dissolution of the layer, and vigorous magnetic stirring was maintained to homogenise the solution. The working electrode was the 6082-aluminium alloy in its different formats, billets or forgings, and a stainless steel sheet was used as the counter electrode. Two conditions were tested at constant current densities of 0.5 A dm^{-2} and 1.5 A dm^{-2}. The reason of using two current densities is to optimise the anodising process, the 1.5 A·dm^{-2} current density is used for anodising aluminium alloys where high wear and corrosion resistance surfaces are required (hard anodising), which is the case of the studied pieces. In the present work, the application of a second, lower current density has been considered, and the anodised films obtained using both conditions were compared, taking into account their potential application on an industrial scale. The use of lower current density would lead to significant cost savings. In both cases, the current was applied for 60 min using a Keithley® 2460 DC power supply. After anodising, samples were subjected to a hot water sealing by immersing the anodised samples in distilled water at 95 °C for 60 min. The samples were then dried in a hot air stream.

2.2. Experimental techniques

The morphology of the tested samples was examined by microscopy techniques. The grain structure was analysed using an Olympus® GX51 optical microscope under polarised light. Beforehand, the samples were polished with 3 mm diamond paste and finished with colloidal silica, and then samples were electrolytically etched in Barker's solution. The intermetallic particles were characterised after etching with a 1 % NaOH solution and Keller's solution using a JEOL® JSM-6510 scanning electron microscope (SEM) equipped with an energy dispersive X-ray analysis (EDS) detector. This technique was also employed to assess the anodised thickness.

The identification of the different phases was performed by X-ray diffraction (XRD) analysis, using a Siemens® X-ray diffractometer with the Cu kα ($\lambda = 0.154$ nm) as anode, and a 2θ range from 20° to 120° and a step size of 0.02°.

The corrosion resistance was studied by electrochemical impedance spectroscopy, EIS, using an Autolab 30 potentiostat from Ecochemie® with a three-electrode arrangement, where the working electrode was the anodised 6082 aluminium alloy ($S = 1.33$ cm^2), a graphite sheet was

Table 1
Chemical composition of tested 6082 Al alloy (wt%) according to EN 573-3 standard.

	Si	Fe	Cu	Mn	Mg	Cr	Zn	Ti	Others	Al
EN AW-6082	0.7–1.3	0.50	0.1	0.40–1.0	0.6–1.2	0.25	0.2	0.1	0.05 (0.15 tot.)	Bal.
VDC	1.21	0.15	0.08	0.59	0.79	0.14	–	0.04		
HDC	1.26	0.26	0.07	0.59	0.79	0.17	0.03	0.03		

the counter-electrode, and a Saturated Calomel Electrode (SCE) was used as the reference electrode. The electrolyte was 0.1 M NaCl solution. All the measurements were carried out at a D.C. potential slightly cathodic to the corrosion potential (E = Ecorr−30 mV) to avoid deviations in the system linearity [41]. A 10 mV_{rms} sinusoidal perturbation was applied. The frequency range was from 100 kHz to 10 mHz with 7 points per decade. To verify the reproducibility of the obtained results, at least three samples were tested for each system.

3. Results and discussion

3.1. Morphological characterisation

3.1.1. Pre-anodised samples

As mentioned above, a microstructural analysis was carried out to identify the differences that may affect the anodising process and, thus, the corrosion resistance of the anodised pieces.

Fig. 1 displays the microstructure observed for cast and forged samples after the electrolytic etching with Baker's solution. The grain structure observed in the VDC billets (Fig. 1a) is characterised by equiaxed dendrites with strong microsegregation. The HDC billets (Fig. 1b) also present equiaxed grains; however, there is no sign of microsegregation, which suggests these billets were subjected to a homogenisation treatment after casting. However, the absence of microsegregation in the HDC billets cannot be ruled out since, at higher magnifications, the dendritic structure is appreciable. Similar grain structures were observed by other researchers [28,40,42]. The grain size is similar in both billets with diameters close to 100 μm, although slightly larger for HDC.

The effect of the forging process is clearly observed in Fig. 1c and d. The typical texture of elongated grains perpendicular to the forging direction can be seen. An additional consequence of the forging process is the elimination of the microsegregation, clearly evidenced by comparing Fig. 1a and Fig. 1c. The texture is maintained throughout the thickness of the sample, although with differences in the produced deformation at different distances from the surface [31]. For this reason, all the replicas were cut in the same area of forgings to avoid differences in the anodising process. The etching with 1 % NaOH revealed the

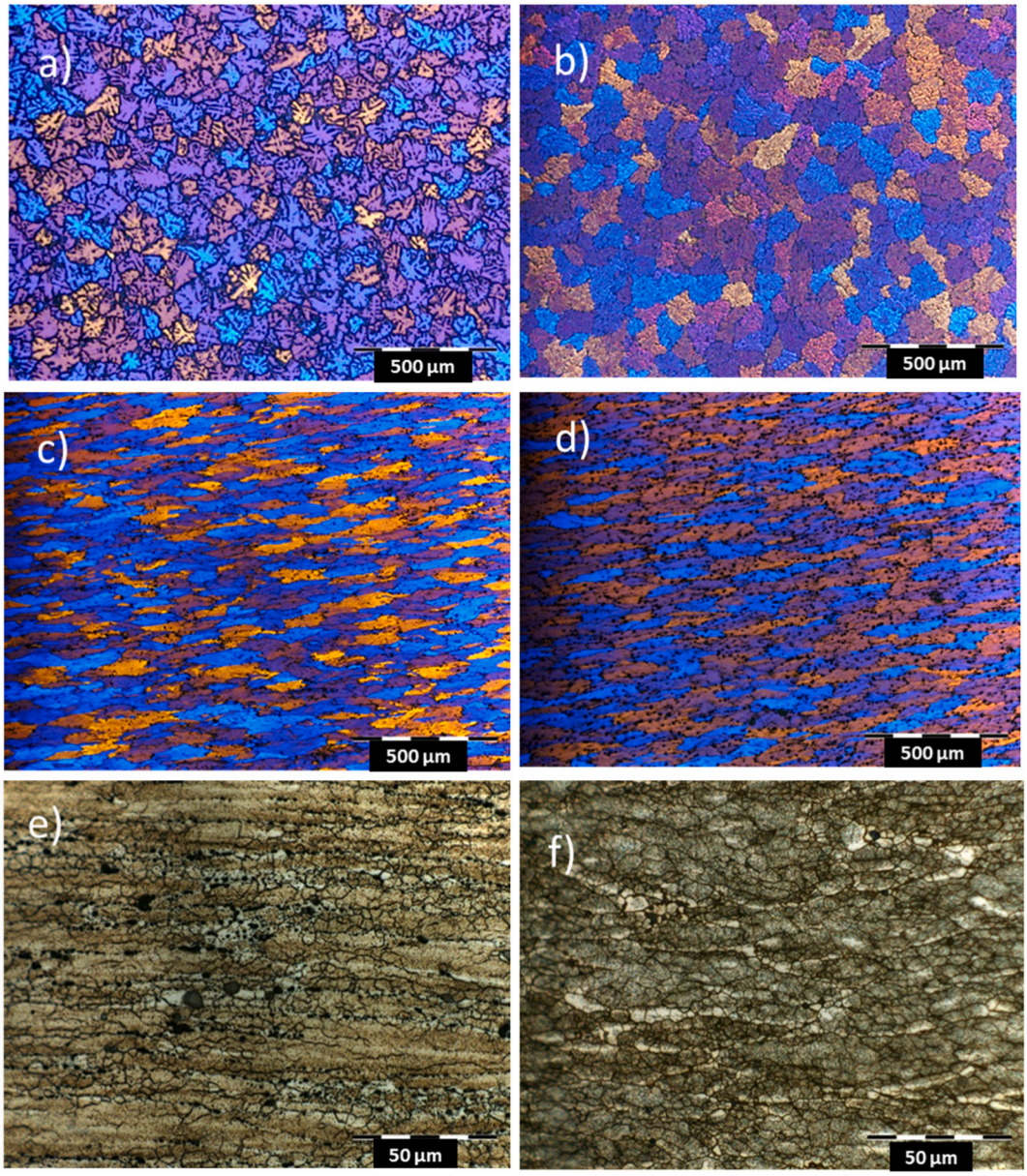

Fig. 1. Grain structure of VDC (a) and HDC (b) cast billets and VDC + T6 (c and e) and HDC + T6 (d and f) forgings.

recrystallised structure of the forged samples as shown in Fig. 1e and Fig. 1f with a smaller grain size than that of the billets, close to 5 μm.

The identification of the intermetallic particles was performed by EDS and X-ray diffraction analysis. Fig. 2 shows a representative image of the microstructure of the cast billets. Three types of particles characteristic of the 6082 alloys were identified. Fe- and Si- rich intermetallic compounds (Fe-IMCs and Si-IMCs) and Mg_2Si precipitates located in the interdendritic regions and at the grain boundaries of the primary α-Al. This structure is in line with that of previous investigations [31,32,42–44].

The morphology and composition of these phases are shown in Fig. 3. The morphology of the light grey particles is displayed in Fig. 3a, Fig. 3b and Fig. 3c. The two first correspond to the Fe-IMCs. However, they differ in morphology and composition. Particles in Fig. 3a have a rounded shape, and the EDS analysis confirms a Fe/Mn atomic ratio close to 1, a high percentage of Al and small amounts of Cr (see Fig. 3e). The X-ray pattern displayed in Fig. 4 identifies these particles as $Al_{17}(Fe_{3.2}Mn_{0.8})Si_2$. Different stoichiometries found in the literature could be assigned to these particles [28,32,42] since they present diffraction peaks in the same positions. Therefore, it can be assumed that these particles belong to the dominant α-AlFeMnSi phase. The needle-shaped particles (Fig. 3b) have a higher silicon content with an Al/Si ratio close to 5, as the EDS spectrum reveals (see Fig. 3e) and can be identified as the β-AlFeSi phase. This was only detected in some VDC billets by EDS, and no signal was recorded by XRD, perhaps due to the low volume fraction, which may be below the XRD detection limit. This phase is mechanically undesirable because it is associated with local crack initiation in surface defects. However, homogenisation treatments in the presence of Mn facilitate its transformation into the α-AlFeMnSi [45].

Fig. 3c shows the morphology of the Si-IMCs, which are also light grey in colour, and rounded in shape. However, their composition does not include Fe and a high Si and Mn content is detected (see Fig. 3e). The XRD analysis shown in Fig. 4 identifies these particles as $Al_{55}Mn_{20}Si_{25}$ in good agreement with the EDS data. G. Mrówka-Nowotnik et al. also identified these particles, although with a slightly different stoichiometry [44].

The dark particles (Fig. 3d) present different morphologies, although the EDS analysis did not show significant differences between the different zones. These particles have been identified as the Mg_2Si phase by XRD analysis (see Fig. 4) and found in both types of billets. The presence of these particles is the basis of the strengthening heat treatment to which this alloy is subjected. This is why only tiny and highly dispersed Mg_2Si particles were found in the forged and heat-treated samples, indicating that the solubilisation process has correctly carried out.

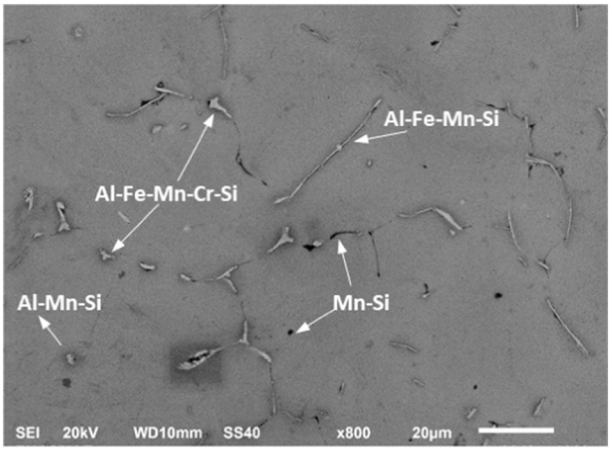

Fig. 2. SEM image showing the microstructure of the 6082 alloy in the as-cast condition including the labelling of the characteristic intermetallic particles.

3.1.2. Anodised samples

The thickness of the AAO films was evaluated by SEM. Fig. 5 shows cross-sectional images obtained for the two anodising conditions on billets.

In the samples anodised at low current density (Fig. 5a and Fig. 5b), low thicknesses, around 6 μm, were obtained. Defects or cracks are also observed throughout the film. These anodising conditions seem not suitable. The reason must be related to the presence of the secondary phases. It has been shown that the growth of the anodic layer on Al-Mg-Si alloys is hindered by the presence of Si particles and Mg- and Fe-rich intermetallics [16,19]. At low current densities, the anodic film forms slowly, and the electrochemical activity of the intermetallic particles favours the anodic film's local dissolution [21]. The film's growth and dissolution rates are two competitive processes. At low current density the growth rate is low, although it must be greater than the dissolution rate, otherwise, there would be no net AAO [14]. However, the result is a soft and thin anodic film with poor barrier properties.

In contrast, using the higher current density, the obtained AAO films look more uniform and with higher thickness, around 15 μm for the VDC billets (Fig. 5c) and close to 20 μm for the HDC billets (Fig. 5d). It seems that a current density of 1.5 $A{\cdot}dm^{-2}$ can counteract the harmful effect of the secondary phases in the anodic film growth.

Embedded intermetallic particles can be distinguished in the oxide layers. A detail of these is shown in Fig. 6a, with the corresponding EDS analysis in Fig. 6b. Fe-rich particles, the dominant α-AlFeMnSi phase, were identified. The surrounding voids are associated with their partial dissolution and oxygen generation during the anodising process. As mentioned above, this type of defect is common in Al-Mg-Si alloys [21–23,29]. However, their presence does not hinder the growth of the layer. It should be noted that Si-rich inclusions were also found in the alumina layer. They probably originated from the preferential dissolution of Mg in the Mg_2Si particles de-alloyed during anodization [21,25].

The thickness of the AAO layer for the forged samples is shown in Fig. 7, considering both current densities. In general, no significant differences were observed regardless of the current density, obtaining thicknesses around 30 μm for both forging alloys. However, a slightly higher thickness seems to be observed for the higher current density conditions. Obtaining similar thicknesses for both current densities may be related to the increased resistance generated by the growth of the layer, which slows down the growth rate. In contrast, the dissolution rate remains constant [1]. The increase in thickness compared to the cast samples is noteworthy, highlighting the significant influence of the microstructure on the anodising process. Furthermore, proper selection of the anodising conditions allows for adequate layer growth and reduces process costs by using lower current densities without reducing layer thickness.

3.2. Electrochemical characterisation

3.2.1. Electrochemical impedance spectroscopy of anodised samples

The electrochemical response of the anodised samples was evaluated by EIS. Fig. 8 depicts the response of anodised billets using a current density of 0.5 $A{\cdot}dm^{-2}$. Impedance values are low with a limit at low frequency around 250 $\Omega{\cdot}cm^2$, which tends to decrease with immersion time. Considering the thin anodic films obtained, these poor barrier properties are expected (see Fig. 5a and Fig. 5b).

Fig. 9 shows the Bode plots obtained for HDC and VDC casting billets at different immersion times using a current density of 1.5 $A{\cdot}dm^{-2}$. The very stable impedance values recorded during the immersion time, mainly for the HDC samples, which remain practically invariant are remarkable. This behaviour indicates the good quality of the anodised film generated and agrees with the cross-sectional images shown in Fig. 5c and Fig. 5d. The impedance modulus at low frequency exhibits a straight line, suggesting a capacitive behaviour, regardless of the type of samples, and the values are very similar, about 10 to 20 $M\Omega{\cdot}cm^2$ at 10 mHz. However, the VDC casting billets show at intermediate frequencies

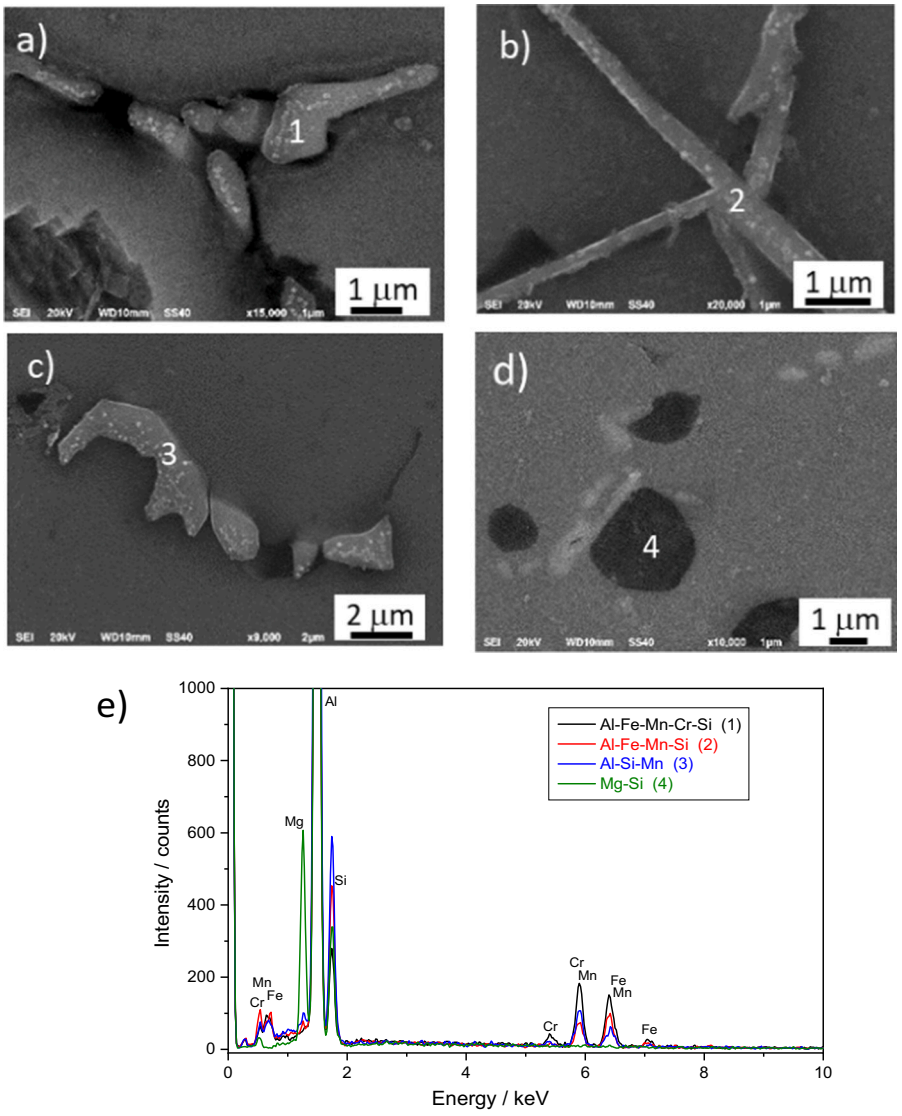

Fig. 3. SEM micrographs of the intermetallic particles identified in the 6082 Al alloy: Al-Fe-Mn-Cr-Si (a), Al-Fe-Mn-Cr-Si (b), Al-Si-Mn (c) and Mg-Si (d). EDS spectra corresponding to the selected areas in the images (e).

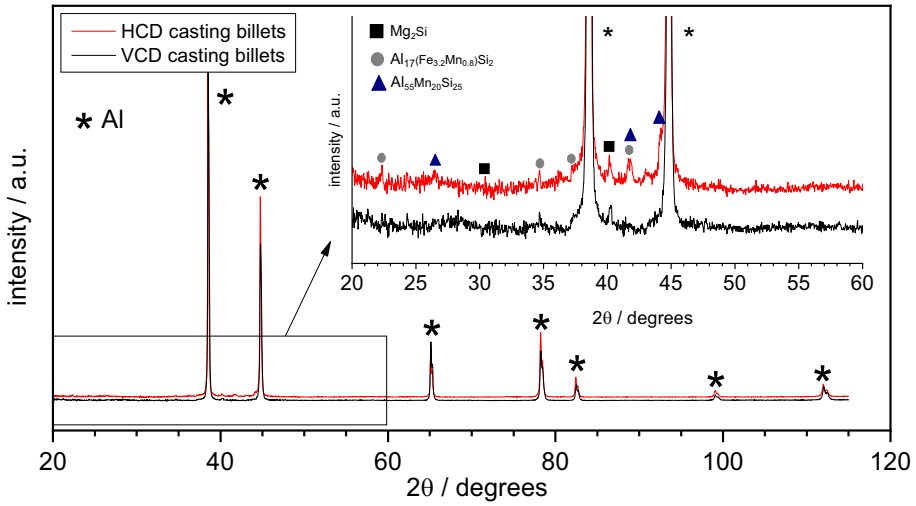

Fig. 4. Diffraction patterns of the 6082 Al alloy in the HCD and VCD billets, including the identification of the main diffraction peaks.

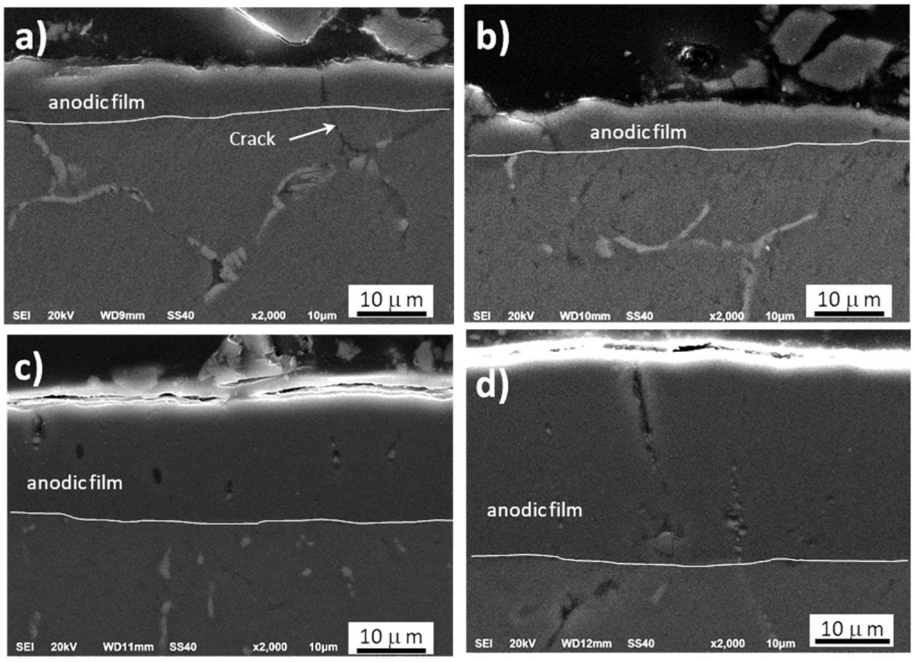

Fig. 5. SEM cross-sectional micrographs of anodised billets at 0.5 A·dm^{-2} current density in VDC (a) and HDC (b), and at 1.5 A·dm^{-2} current density in VDC (c) and HDC (d).

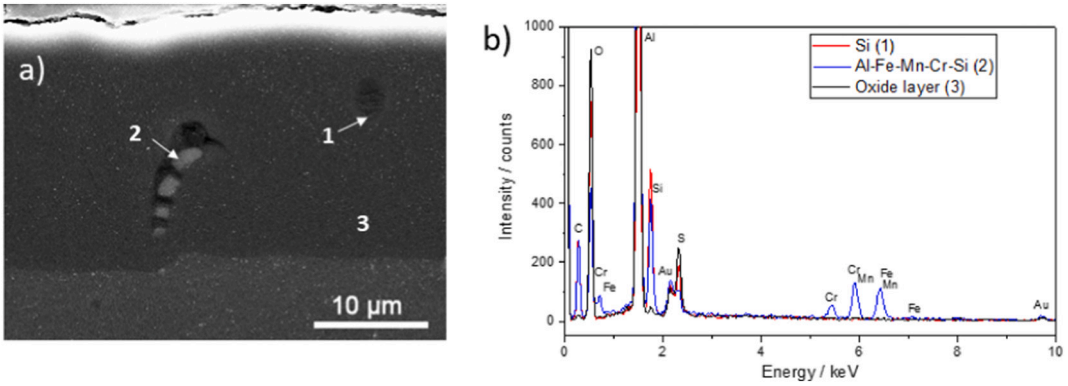

Fig. 6. SEM cross-sectional micrograph of anodised billets at 1.5 A·dm^{-2} showing the particles embedded in the aluminium oxide layer (a) and their EDS analysis (b).

impedance values about one order of magnitude lower than those for HDC samples.

This impedance behaviour has been modelled using the electrical equivalent circuit (EEC) depicted in Fig. 10a. This EEC has often been used to characterise anodised aluminium alloys [46–50] that considers infinite the resistance associated with the non-porous fraction of the coating (resistance not represented, in parallel with C_{HF}). The high frequency time constant, $R_{HF}C_{HF}$, is related to the resistance of the outer layer in contact with the electrolyte (layer generated during the sealing treatment) and the geometric capacitance associated with the layer thickness. The second time constant, R_pC_p, appears at intermediate frequencies and is ascribed to the dielectric properties of the filled pores. At low frequencies, the third time constant, R_bC_b, accounts for the compact anodised layer at the bottom of the pores. The time constants are affected by a Cole-Cole parameter, α_i, which accounts for the dispersion of the corresponding time constants [51].

The total impedance is given by Eq. (1):

$$Z = R_e + \frac{R_{HF}}{\frac{1}{1+\frac{Z_p+Z_{LF}}{R_{HF}}} + (j\omega R_{HF}C_{HF})^{\alpha_{HF}}} \quad (1)$$

$$\text{Being } Z_p = \frac{R_p}{1+(j\omega R_pC_p)^{\alpha_p}} \text{ and } Z_b = \frac{R_b}{1+(j\omega R_bC_b)^{\alpha_b}} \quad (2)$$

The good agreement between the experimental measurements and the fitted results is depicted in Fig. 10b. In this figure, the straight line at low frequency, characteristic of blocking electrodes, can also be appreciated.

The evolution of the associated parameters is shown in Fig. 11. In general, all the parameters are relatively stable, as expected, considering the impedance data. The HDC billets exhibit much higher R_{HF} values and lower C_{HF} values than the VDC billets, which is consistent with a thicker anodised film (see Fig. 5d). Regarding the second time constant, the R_p values are equal for both types of billets, with very stable values around 4×10^5 Ω·cm^2. On the contrary, the capacitance values are very different; thus, the Cp values for the HDC billets are in the order of 0.1 µF·cm^{-2}, while the VDC billets give values around 3 µF·cm^{-2}. This difference must be related to the degree of hydration of the species inside the pores, mainly alumina. As mentioned, the R_{HF} is lower in VDC billets, facilitating electrolyte absorption during sealing. The consequence would be a more significant amount of hydrated alumina filling the pores and some extra water being partially bound to the alumina,

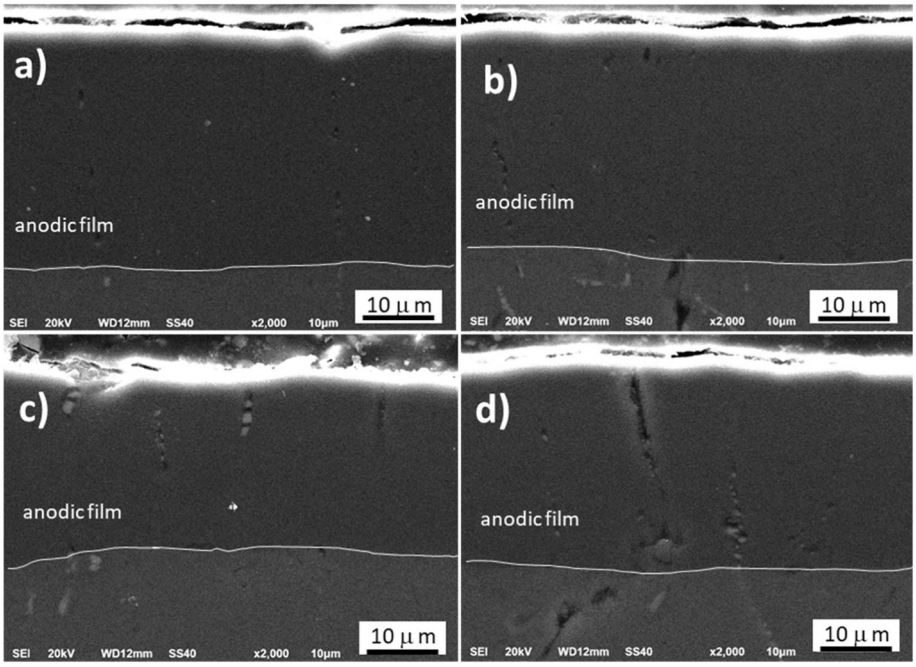

Fig. 7. SEM cross-sectional micrographs of anodised forged and heat treated (T6) samples using 0.5 A·dm^{-2} current density in VDC (a) and HDC (b), and at 1.5 A·dm^{-2} current density in VDC (c) and HDC (d).

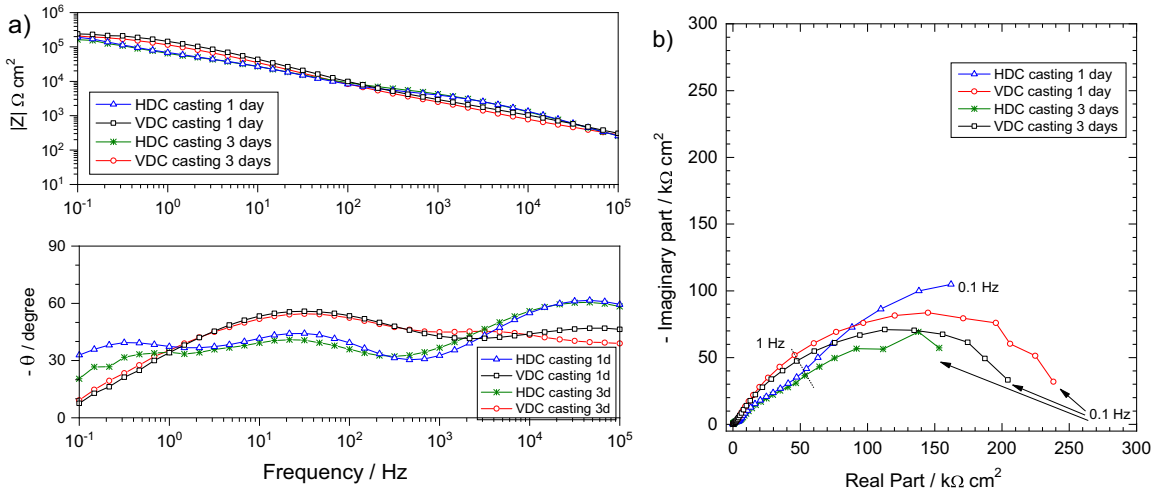

Fig. 8. Bode (a) and Nyquist (b) plots obtained for HDC and VDC billets at 1 and 3 days of immersion in 0.1 M NaCl solution using a current density of 0.5 A·dm^{-2} for the anodising procedure.

increasing the permittivity and, therefore, the capacitance of the porous layer.

The properties of the barrier layer at the pore bottoms, R_bC_b, are shown in Fig. 11c and Fig. 11d. For HDC billets, both parameters show again very stable values, with a slight increase in R_b and a decrease in C_b, which may indicate a slight thickening of this compact film. For the VDC billets, the evolution of R_b is characterised by an initial decline, which suggests a specific interaction between the electrolyte and this layer; this interaction may favour the blocking of possible defects in this layer, so the R_b increases with longer immersion periods. The evolution observed in the capacitance supports this interpretation, with an initial increase followed by a stabilisation. After this stabilisation, the C_b values are similar for both types of billets, about 1 µF·cm^{-2}. Considering a dielectric constant of 10 for the anhydrous alumina, the thickness of the barrier layer would be about 10 nm. This result aligns with those obtained by other authors [24,52].

These results indicate that, even though the total impedance is similar in both cases, the morphology of the anodised film is different depending on the stage of the alloy. Fine equiaxed dendrites with strong microsegregation characterise the grains structure observed for VDC billets (see Fig. 1a). In the same way that the presence of second phase particles affects the surface reactivity of the aluminium alloys and thus, the anodisation [19,25], it is reasonable to assume that the microsegregation (chemical heterogeneity) negatively influences the growth of the oxide film, additional local dissolution may take place which acts as a "leakage", resulting in a thinner anodic oxide film [21]. This hypothesis is corroborated by the lower thickness measured for the AAO layer in the VDC billets (Fig. 5c).

HDC and VDC + T6 heat treatment forgings were also anodised, and their electrochemical behaviour was evaluated by EIS. In this case, the two anodising conditions (current densities of 1.5 A·dm^{-2} and 0.5 A·dm^{-2}) generated a stable anodic film. Fig. 12 illustrates an example of

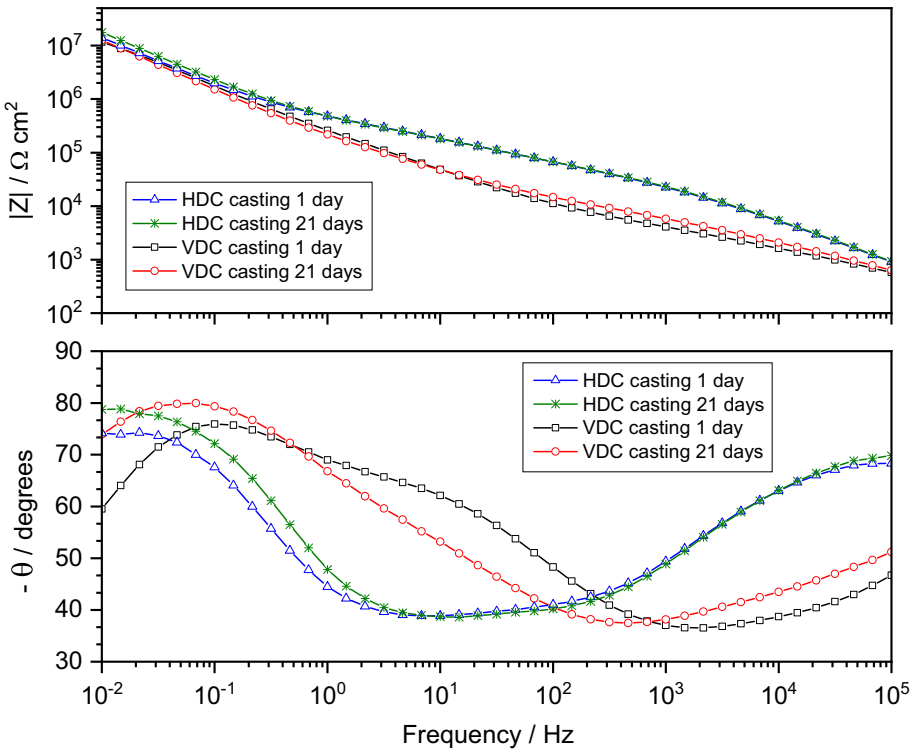

Fig. 9. Bode plots (modulus and phase angle) obtained for VDC and HDC casting billets for 1 day and 21 days immersion time in 0.1 M NaCl solution.

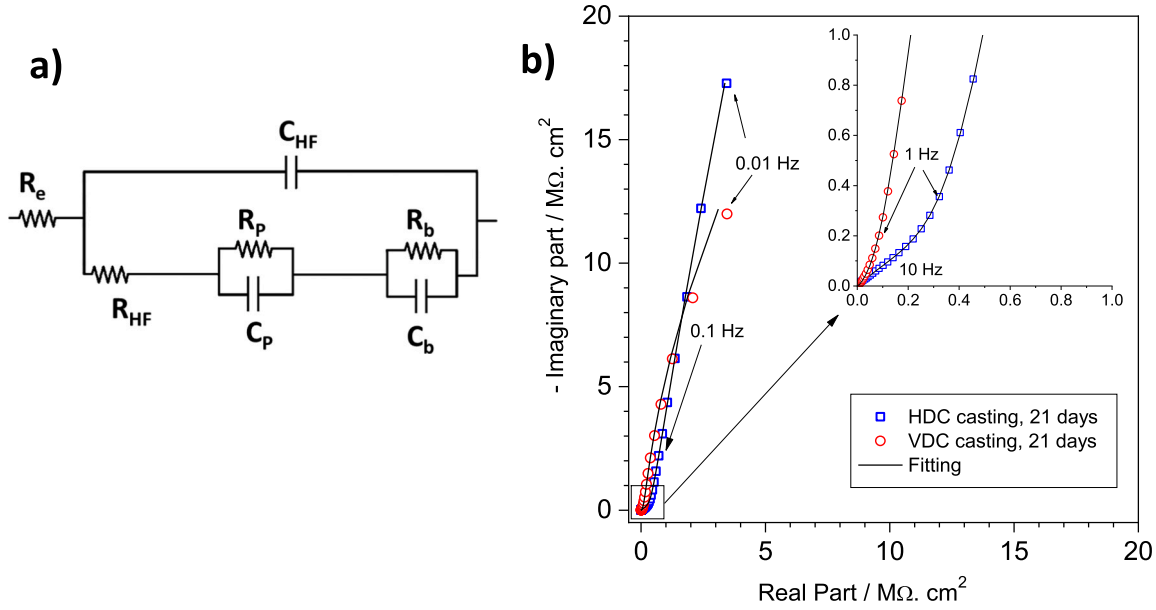

Fig. 10. Electrical equivalent circuit (EEC) used to model the impedance measurements obtained for the anodised 6082 aluminium alloys. The physical meaning is explained in the text (a). Experimental and fitted Nyquist plots corresponding to HDC and VDC casting billets after 21 days of immersion in 0.1 M NaCl solution (b).

the impedance plots obtained under these two conditions.

As can be seen, the response of both films is very similar; only minor differences are observed in the high frequency range. The higher impedance modulus observed in the films generated at higher current densities indicates a higher pore wall thickness. This result is as expected [19]. However, the overall impedance is similar in both cases. Based on this and considering that using lower current densities represents an important saving for industrial purposes, the present study will focus on anodic films generated at 0.5 A·dm^{-2}. Fig. 13 shows the Bode and Nyquist plots acquired at different immersion times using the latter conditions.

The impedance measurements indicate the same behaviour for both types of forgings with very similar impedance plots. They follow the characteristic pattern of anodised samples with no low frequency limit, associated with a blocked electrode feature. In the phase angle, minor differences are observed at high and medium frequencies, where the pores wall and porous layer responses are located.

The measurements were modelled using the EEC depicted in Fig. 10a, whose physical meaning has already been explained. The evolution of the fitting parameters is shown in Fig. 14.

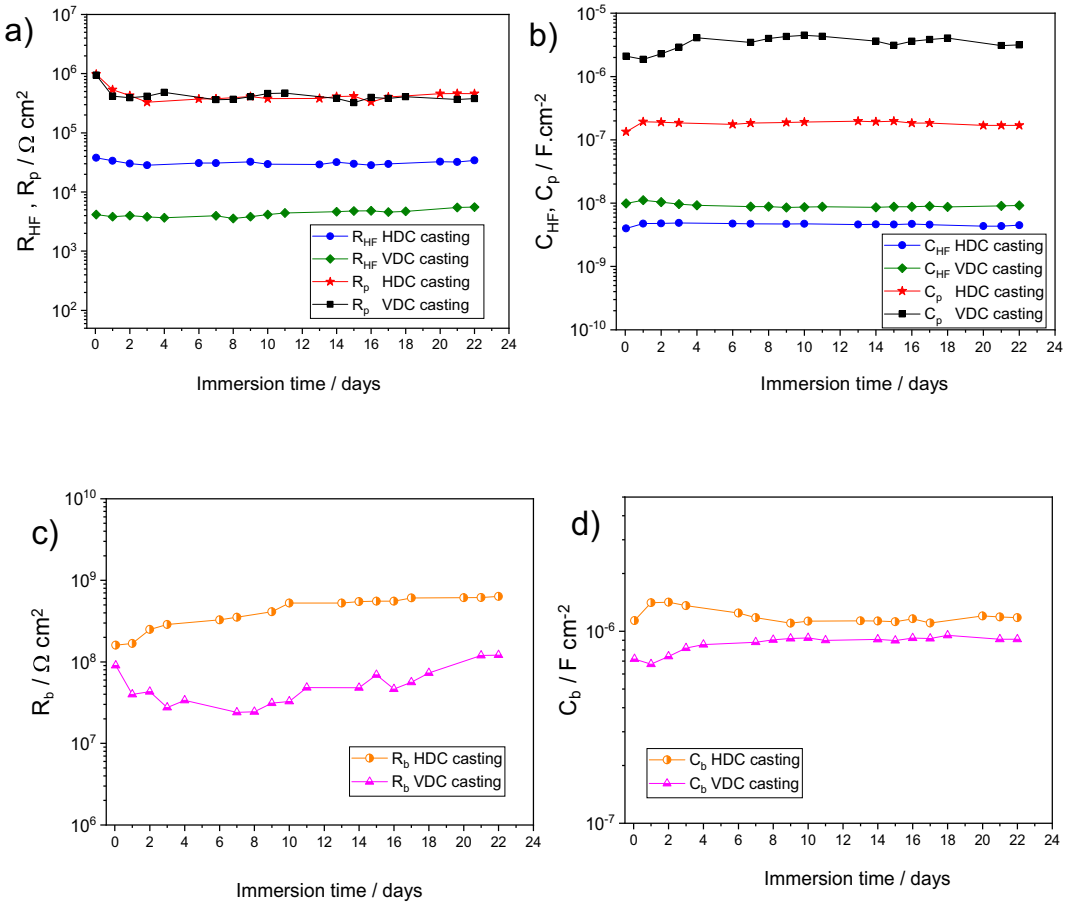

Fig. 11. Evolution of the fitting parameters corresponding to R_{HF} and R_p (a), C_{HF} and C_p (b), R_b (c) and C_b (d) for HDC and VDC casting billets as a function of immersion time.

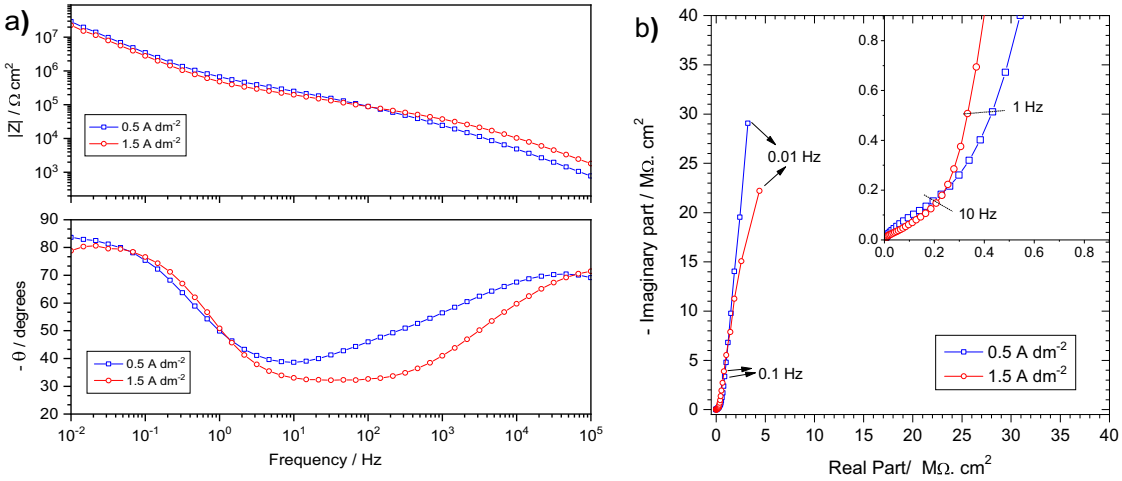

Fig. 12. Bode (a) and Nyquist (b) plots obtained for HDC + T6 forgings after 20 days of immersion in a 0.1 M NaCl solution, using the two anodising conditions.

As with the billets, the fitting parameter values are quite stable throughout the immersion time, indicating the generation of a stable film. However, unlike the billets, no significant differences are observed in the forgings depending on the type of initial billet (HDC or VDC).

A consequence of the forging procedure is the improvement of the chemical homogeneity of the pieces [31]. This may explain the increase observed in the R_{HF} values for VDC forgings compared to those of VDC billets. Moreover, these high R_{HF} values also explain the C_p values obtained for the VDC forgings, around 100 nF·cm^{-2}, in the same order of magnitude as those for HDC forgings or billets. These results corroborate the better barrier against electrolyte absorption during the sealing process. The low frequency time constant, associated with the compact pores bottom layer, is characterised by huge values of R_b, in the order of GΩ·cm^2, in both cases. It should be noted, however, that these values are affected by some uncertainty since the corresponding characteristic frequencies are around 10^{-5} Hz, far from the lowest scanned frequency

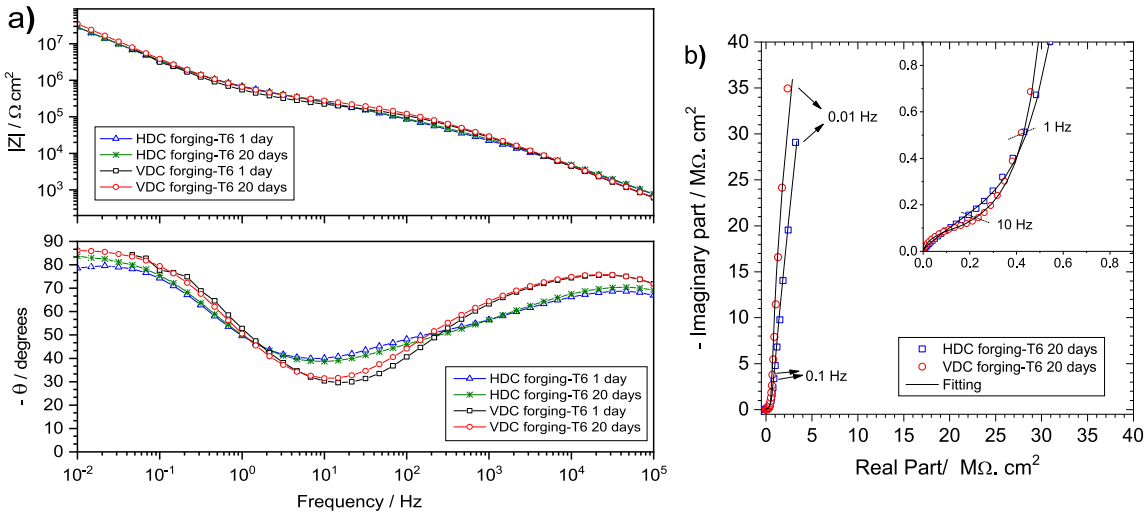

Fig. 13. Evolution of the Bode plots for VDC and HDC forging-T6 pieces with immersion time in 0.1 M NaCl solution (a). Experimental and fitted Nyquist plots corresponding to both types of pieces after 20 days of immersion in 0.1 M NaCl solution using the EEC shown in Fig. 10a (b).

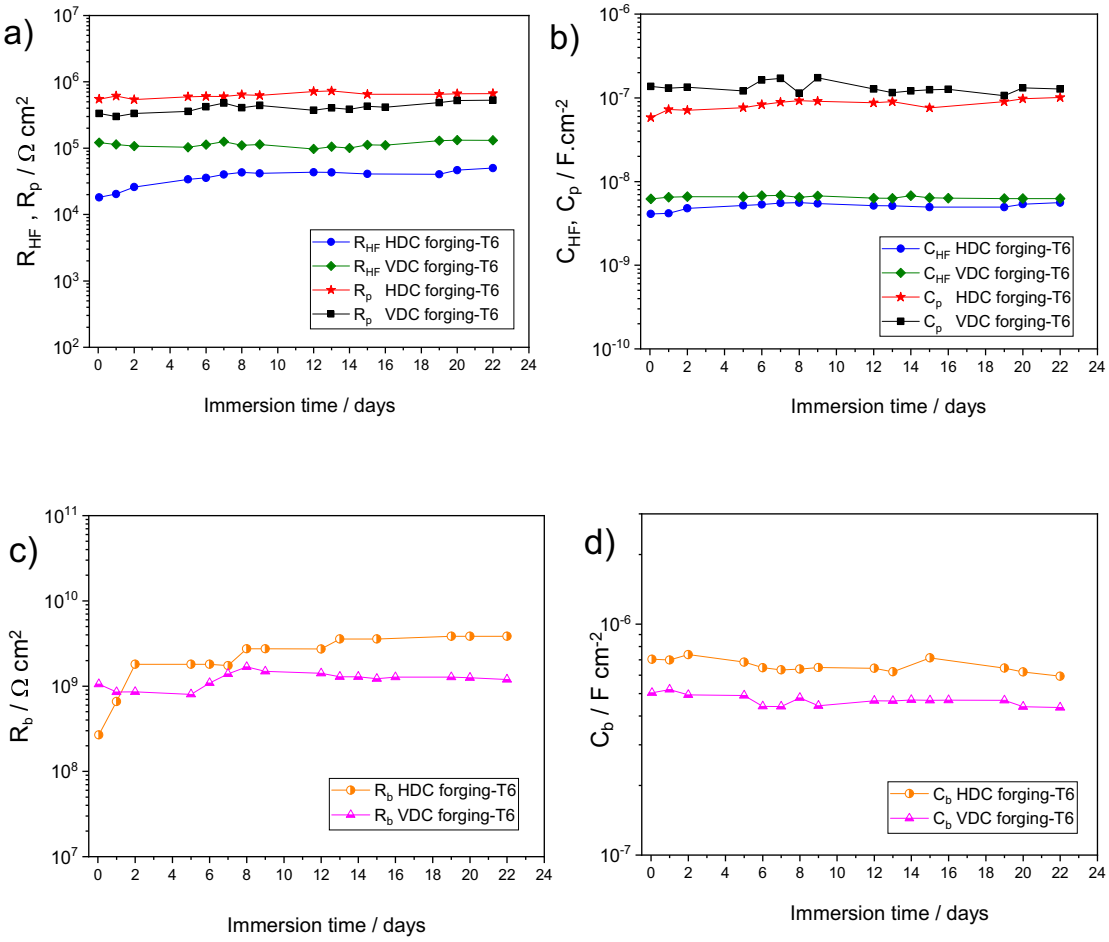

Fig. 14. Evolution of the fitting parameters corresponding to R_{HF} and R_p (a), C_{HF} and C_p (b), R_b (c) and C_b (d) for HDC and VDC forging + T6 pieces with immersion time.

used in these experiments. From the capacitance values, C_b, the thickness of this layer can be estimated to be about 25 nm. The higher values with respect to that of the billets agree with the conclusions of other researchers who point to generating thicker anodic layers on machined substrates than as-cast ones [16].

3.2.2. *Electrochemical behaviour of the intermetallic particles*

The EIS results reveal significant differences in the AAO films generated between the billets and the forgings + T6 formats. The growth of this oxide layer is influenced by the presence of the intermetallic particles, namely their size and/or distribution in the α-Al matrix before

the anodising process, which should affect the growth of the oxide layer. To elucidate this point, polished samples of billets and forgings + T6 were immersed in 0.1 M NaCl, then anodically polarised at 1 $mV{\cdot}s^{-1}$ up to 400 mV above the OCP. Fig. 15 shows the different attack morphologies.

Fig. 15a shows the corrosion morphology of the areas where severe attack was observed in the billets. Large pits corresponding to matrix dissolution were observed, although the corrosion must initiate at the grain boundary, where the IMC particles are preferentially located. Fig. 15b is a detail of this area. The presence of unaltered Fe-IMCs and intense attack in the surrounding area can be appreciated, with no evidence of Mg_2Si. These particles are anodic with respect to the matrix; thus, corrosion initiates on their surface. However, as corrosion progresses, preferential dissolution of Mg occurs and, therefore, silicon enrichment changes the polarity, leading to the dissolution of the matrix at the perimetry of these particles [53]. Fig. 15c illustrates an area with a slight attack; the dark particles correspond to Si as the EDS analysis confirmed (Fig. 15d). The oxygen signal suggests the surface oxidation of these particles. Although the size of these particles was not assessed, it can be concluded from the different micrographs taken that they have a length of several micrometers. During the anodising process, they can be embedded in the oxide layer, but not easily, leading to discontinuities in the anodic film or even inhibiting its growth [16].

The attack morphology of forged + T6 samples is different, as shown in Fig. 15e and Fig. 15f. The pit size is smaller, and intergranular corrosion is appreciated, revealing the smaller grains generated in the recrystallisation process that takes place during the forging and heat treatment. This structure was already shown in Fig. 1e and Fig. 1f. The solubilisation of the Mg_2Si particles and their subsequent precipitation during the artificial ageing treatment produce very fine precipitates, in the nanometric scale, within the grain as well as at the grain boundary. This homogeneous distribution, together with the small size, favours the formation of a uniform and continuous oxide layer during the anodising process, because the oxidation front can easily embed these small particles [19].

4. Conclusions

The results extracted from the present work highlighted the strong effect of surface morphology on the generation of the anodic layer during the anodising process.

Regardless of HDC or VDC technology, the as-cast samples generated a thin anodic film with poor barrier properties at the low current density of 0.5 $A{\cdot}dm^{-2}$. This was attributed to the similar growth and dissolution rates of the film layer due to the electrochemical activity of the intermetallic particles that favour local dissolution of the anodic film. At higher current densities, 1.5 $A{\cdot}dm^{-2}$, a uniform and thicker AAO layer was generated on both types of billets. High current densities could overcome the local dissolution effect of the secondary phases. However, the oxide film thickness was lower for VDC billets. The differences were explained considering the marked microsegregation observed in the VDC billets, which was not seen in the HDC billets. The EIS

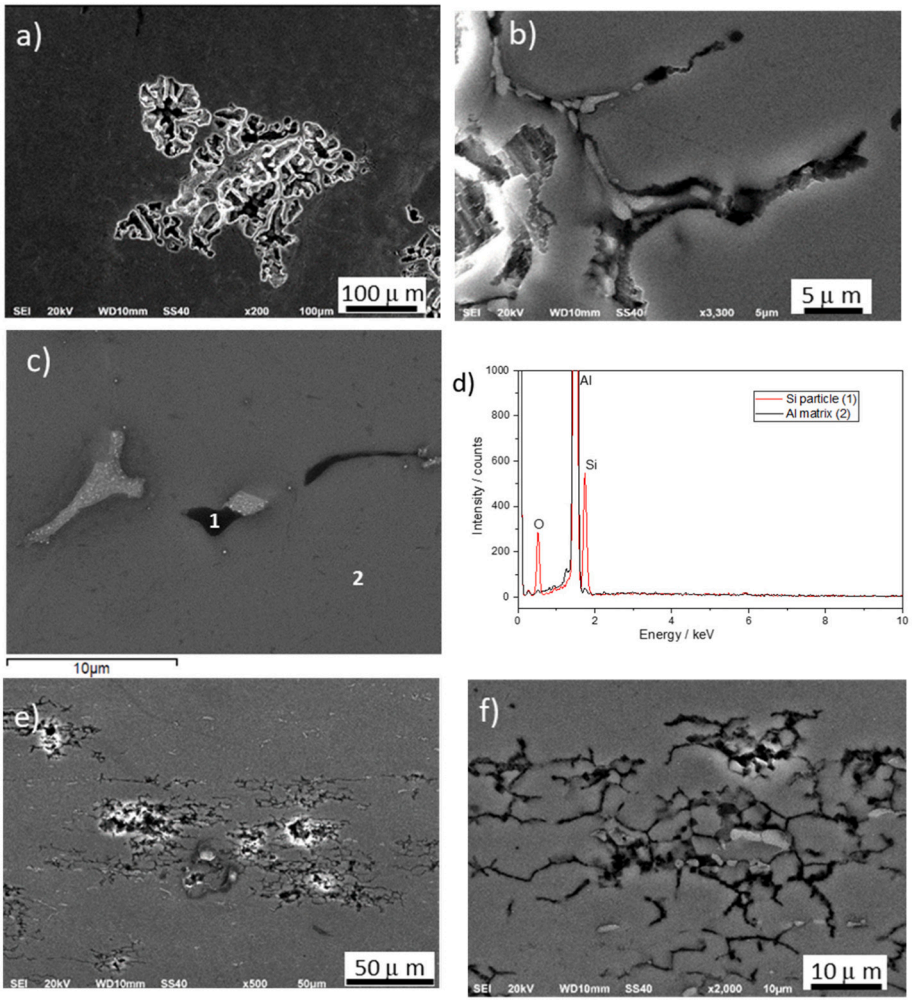

Fig. 15. Corrosion morphology of the 6082 Al alloy under different formats: billet in an area of severe attack (a, b), area with a slight attack of the billet (c), the EDS corresponding to image 14c (d) and forging + T6 with a severe attack (e, f).

measurements remained stable throughout the immersion test, which corroborated the generation of a stable film. However, the lower values observed at high and middle frequency ranges for VDC billets confirmed the negative effect of the microsegregation.

Forging and heat treatment beneficiated the anodising process, reaching AAO layer thicknesses in the order of 30 μm even for the lowest current density. The improvements had been attributed, on the one hand, to the forging process, which enhanced the chemical homogeneity of the pieces, and on the other hand, to the heat treatment, which solubilised and homogeneously redistributed the Mg_2Si particles in the aluminium matrix, allowing a more homogeneous current distribution on the surface during anodising. The good corrosion resistance was confirmed by the high impedance values recorded even at long immersion times. The values were similar for both types of forged pieces, which corroborates the elimination of the structural differences of the billets.

The results show that the microstructure and heat treatment largely determine the anodising conditions of the 6082 Al alloy. Furthermore, optimisation of the anodising conditions not only leads to a higher growth rate of the oxide layer but also helps reduce the cost of the process, as similar thicknesses were obtained at different current densities without detrimental effects on the barrier properties.

CRediT authorship contribution statement

B. Díaz: Validation, Methodology. **R. Figueroa:** Writing – original draft, Investigation, Conceptualization. **X.R. Nóvoa:** Writing – review & editing, Supervision. **C. Pérez:** Writing – review & editing, Visualization, Conceptualization. **C. Pérez-Betanzos:** Methodology. **S. Valverde-Pérez:** Resources, Methodology.

Declaration of competing interest

The authors declare that they have no known competing financial interests or personal relationships that could have appeared to influence the work reported in this paper.

Acknowledgements

The authors acknowledge the Universidade de Vigo for Open Access Funding provided by CISUG Agreement, and the Xunta de Galicia (Consellería de Cultura, Educación e Universidade) for grant Nr. ED431B 2021/14.

References

[1] M.P. Martínez-Viademonte, S.T. Abrahami, T. Hack, M. Burchardt, H. Terryn, A review on anodizing of aerospace aluminum alloys for corrosion protection, Coatings 10 (2020) 1–30, https://doi.org/10.3390/coatings10111106.
[2] R. del Olmo, U. Tiringer, I. Milošev, P. Visser, R. Arrabal, E. Matykina, J.M.C. Mol, Hybrid sol-gel coatings applied on anodized AA2024-T3 for active corrosion protection, Surf. Coat. Technol. 419 (2021) 127251, https://doi.org/10.1016/j.surfcoat.2021.127251.
[3] J.A. Moreto, O. Gamboni, C.O.F.T. Rucherf, F. Romagnoli, M.F. Moreira, F. Beneduce, W.W. Bose Filho, Corrosion and fatigue behavior of new Al alloys, Procedia Eng. 10 (2011) 1521–1526, https://doi.org/10.1016/j.proeng.2011.04.254.
[4] B. Wielage, G. Alisch, T. Lampke, D. Nickel, Anodizing - a key for surface treatment of aluminium, Key Eng. Mater. 384 (2008) 263–281, https://doi.org/10.4028/www.scientific.net/kem.384.263.
[5] M. Whelan, K. Barton, J. Cassidy, J. Colreavy, B. Duffy, Corrosion inhibitors for anodised aluminium, Surf. Coat. Technol. 227 (2013) 75–83, https://doi.org/10.1016/j.surfcoat.2013.02.029.
[6] D. Raps, T. Hack, J. Wehr, M.L.L. Zheludkevich, A.C.C. Bastos, M.G.S.G.S. Ferreira, O. Nuyken, Electrochemical study of inhibitor-containing organic–inorganic hybrid coatings on AA2024, Corros. Sci. 51 (2009) 1012–1021, https://doi.org/10.1016/j.corsci.2009.02.018.
[7] S. Liu, J. Tian, W. Zhang, Fabrication and application of nanoporous anodic aluminum oxide: a review, Nanotechnology 32 (2021) 222001, https://doi.org/10.1088/1361-6528/abe25f.
[8] W. Zhu, Y. Deng, X. Guo, Influence of adjusting the anodizing and aging sequences on the microstructure, fatigue property and corrosion resistance of anodized AA6082 alloys, Mater. Charact. 189 (2022) 111941, https://doi.org/10.1016/j.matchar.2022.111941.
[9] S.T. Abrahami, J.M.M. de Kok, H. Terryn, J.M.C. Mol, Towards Cr(VI)-free anodization of aluminum alloys for aerospace adhesive bonding applications: a review, Front. Chem. Sci. Eng. (2017) 1–18, https://doi.org/10.1007/s11705-017-1641-3.
[10] M. Kendig, S. Jeanjaquet, R. Addison, J. Waldrop, Role of hexavalent chromium in the inhibition of corrosion of aluminum alloys, Surf. Coat. Technol. 140 (2001) 58–66, https://doi.org/10.1016/S0257-8972(01)01099-4.
[11] J. Lee, Y. Kim, H. Jang, W. Chung, Cr2O3 sealing of anodized aluminum alloy by heat treatment, Surf. Coat. Technol. 243 (2014) 34–38, https://doi.org/10.1016/J.SURFCOAT.2012.05.071.
[12] W. Lee, S.J. Park, Porous anodic aluminum oxide: anodization and templated synthesis of functional nanostructures, Chem. Rev. 114 (2014) 7487–7556, https://doi.org/10.1021/cr500002z.
[13] T. Vignoli Machado, P. Atz Dick, G.H. Knörnschild, L.F.P. Dick, The effect of different carboxylic acids on the sulfuric acid anodizing of AA2024, Surf. Coat. Technol. 383 (2020) 125283, https://doi.org/10.1016/j.surfcoat.2019.125283.
[14] J. Cabral-Miramontes, F. Almeraya-Calderón, F.E. López, M. Lara Banda, J. Olguín-Coca, L.D. López-León, I. Castañeda-Robles, M.Á.E. Alcalá, P. Zambrano-Robledo, C. Gaona-Tiburcio, Citric acid as an alternative to sulfuric acid for the hard-anodizing of aa6061, Metals (Basel) 11 (2021) 1838, https://doi.org/10.3390/met11111838.
[15] P. Li, L. Qin, B. Chen, S. Zhang, Y. Zhu, B. Wang, X. Zhu, The role of fluoride and phosphate anions in the formation of anodic titanium dioxide nanotubes, Electrochem. Commun. 158 (2024) 107641, https://doi.org/10.1016/j.elecom.2023.107641.
[16] G. Scampone, G. Timelli, Anodizing Al–Si foundry alloys: a critical review, Adv. Eng. Mater. 24 (2022) 2101480, https://doi.org/10.1002/adem.202101480.
[17] V. Moutarlier, M.P. Gigandet, L. Ricq, J. Pagetti, Electrochemical characterisation of anodic oxidation films formed in presence of corrosion inhibitors, Appl. Surf. Sci. 183 (2001) 1–9, https://doi.org/10.1016/S0169-4332(01)00364-6.
[18] I. Tsangaraki-Kaplanoglou, S. Theohari, T. Dimogerontakis, N. Kallithrakas-Kontos, Y.M. Wang, H.H. Kuo, S. Kia, Effect of alloy types on the electrolytic coloring process of aluminum, Surf. Coat. Technol. 200 (2006) 3969–3979, https://doi.org/10.1016/j.surfcoat.2005.02.174.
[19] L.E. Fratila-Apachitei, H. Terryn, P. Skeldon, G.E. Thompson, J. Duszczyk, L. Katgerman, Influence of substrate microstructure on the growth of anodic oxide layers, Electrochim. Acta 49 (2004) 1127–1140, https://doi.org/10.1016/j.electacta.2003.10.024.
[20] T.-S. Shih, T.-H. Lee, Y.-J. Jhou, The effects of anodization treatment on the microstructure and fatigue behavior of 7075-T73 aluminum alloy, Mater. Trans. 55 (2014) 1280–1285, https://doi.org/10.2320/matertrans.M2014121.
[21] F. Zhang, J.-O. Nilsson, J. Pan, In situ and operando AFM and EIS studies of anodization of Al 6060: influence of intermetallic particles, J. Electrochem. Soc. 163 (2016) C609–C618, https://doi.org/10.1149/2.0061610jes.
[22] H. Wu, Y. Ma, W. Huang, X. Zhou, K. Li, Y. Liao, Z. Wang, Z. Liang, L. Liu, Effect of iron-containing intermetallic particles on film structure and corrosion resistance of anodized AA2099 alloy, J. Electrochem. Soc. 165 (2018) C573–C581, https://doi.org/10.1149/2.1361809jes.
[23] B. Zhu, M. Fedel, N.-E. Andersson, P. Leisner, F. Deflorian, C. Zanella, Effect of Si content and morphology on corrosion resistance of anodized cast Al-Si alloys, J. Electrochem. Soc. 164 (2017) C435–C441, https://doi.org/10.1149/2.1631707jes.
[24] M. García-Rubio, P. Ocón, M. Curioni, G.E. Thompson, P. Skeldon, A. Lavía, I. García, Degradation of the corrosion resistance of anodic oxide films through immersion in the anodising electrolyte, Corros. Sci. 52 (2010) 2219–2227, https://doi.org/10.1016/j.corsci.2010.03.004.
[25] A.K. Mukhopadhyay, A.K. Sharma, Influence of Fe-bearing particles and nature of electrolyte on the hard anodizing behaviour of AA 7075 extrusion products, Surf. Coat. Technol. 92 (1997) 212–220, https://doi.org/10.1016/S0257-8972(97)00102-3.
[26] A. Collazo, I. Ezpeleta, R. Figueroa, X.R. Nóvoa, C. Pérez, Corrosion protection properties of anodized AA2024T3 alloy sealing with organic-based species, Prog. Org. Coat. 147 (2020) 105779, https://doi.org/10.1016/j.porgcoat.2020.105779.
[27] F. Guo, Y. Cao, K. Wang, P. Zhang, Y. Cui, Z. Hu, Z. Xie, Effect of the anodizing temperature on microstructure and tribological properties of 6061 aluminum alloy anodic oxide films, Coatings 12 (2022) 314, https://doi.org/10.3390/coatings12030314.
[28] J.M. Yu, T. Hashimoto, H.T. Li, N. Wanderka, Z. Zhang, C. Cai, X.L. Zhong, J. Qin, Q.P. Dong, H. Nagaumi, X.N. Wang, Formation of intermetallic phases in unrefined and refined AA6082 Al alloys investigated by using SEM-based ultramicrotomy tomography, J. Mater. Sci. Technol. 120 (2022) 118–128, https://doi.org/10.1016/j.jmst.2022.02.007.
[29] L. Winter, T. Lampke, Fatigue resistance of an anodized and hardanodized 6082 aluminum alloy depending on the coating thickness in the high cycle regime, Adv. Eng. Mater. 25 (2023) 2300394, https://doi.org/10.1002/adem.202300394.
[30] L. Yang, D. Bai, D. Wang, C. Liu, S. Yang, G. Huang, Effect of aging temperature on microstructure and corrosion behavior of 6082 aluminum alloy, Mater. Today Commun. 36 (2023) 106583, https://doi.org/10.1016/j.mtcomm.2023.106583.
[31] Y. Birol, E. Gokcil, M.A. Guvenc, S. Akdi, Processing of high strength EN AW 6082 forgings without a solution heat treatment, Mater. Sci. Eng. A 674 (2016) 25–32, https://doi.org/10.1016/j.msea.2016.07.062.
[32] N. Kumar, S. Goel, R. Jayaganthan, H.G. Brokmeier, Effect of solution treatment on mechanical and corrosion behaviors of 6082-T6 Al alloy, Metallogr. Microstruct. Anal. 4 (2015) 411–422, https://doi.org/10.1007/s13632-015-0219-z.

[33] B. Zhou, L. Yang, S.B. Yang, D. Bai, O. Olugbade, G.Z. Huang, Stress corrosion behavior of 6082 aluminum alloy, Mater. Corros. 71 (2020) 1194–1205, https://doi.org/10.1002/maco.201911433.
[34] L. Winter, T. Lampke, Influence of hydrothermal sealing on the high cycle fatigue behavior of the anodized 6082 aluminum alloy, Coatings 12 (2022) 1070, https://doi.org/10.3390/coatings12081070.
[35] D. Caliari, G. Timelli, B. Zabala, A. Igartua, Microstructural and tribological investigations of diecast and hard anodized AlSiCu alloys, Surf. Coat. Technol. 352 (2018) 462–473, https://doi.org/10.1016/j.surfcoat.2018.07.084.
[36] Y. Birol, O. Ilgaz, Effect of cast and extruded stock on grain structure of en AW 6082 alloy forgings, Mater. Sci. Technol. (United Kingdom). 30 (2014) 860–866, https://doi.org/10.1179/1743284713Y.0000000407.
[37] J. Shan, D. Hou, J. Zhang, X. Xin, G. Cao, H. Genzhe, Effects of the extrusion ratio on the intergranular corrosion behaviour of 6082 aluminium alloy, Mater. Corros. 69 (2018) 365–375, https://doi.org/10.1002/maco.201709688.
[38] G.C. Nzebuka, C.O. Ufodike, C.P. Egole, Influence of various aspects of low-Reynolds number turbulence models on predicting flow characteristics and transport variables in a horizontal direct-chill casting, Int. J. Heat Mass Transf. 179 (2021) 121648, https://doi.org/10.1016/j.ijheatmasstransfer.2021.121648.
[39] AENOR, UNE-EN 573-3:2014. Aluminium and Aluminium Alloys - Chemical Composition and Form of Wrought Products - Part 3: Chemical Composition and Form of Products, Http://Www.Ca.Aenor.Es/. (2014) 36.
[40] F. Zupanič, M. Steinacher, S. Žist, T. Bončina, Microstructure and properties of a novel Al-Mg-Si alloy aa 6086, Metals (Basel) 11 (2021) 1–14, https://doi.org/10.3390/met11020368.
[41] L. Domingues, J.C.S. Fernandes, M. Da Cunha Belo, M.G.S. Ferreira, L. Guerra-Rosa, Anodising of Al 2024-T3 in a modified sulphuric acid/boric acid bath for aeronautical applications, Corros. Sci. 45 (2003) 149–160, https://doi.org/10.1016/S0010-938X(02)00082-3.
[42] Y. Birol, S. Akdi, Cooling slope casting to produce en AW 6082 forging stock for manufacture of suspension components, Trans. Nonferrous Met. Soc. China (English Ed) 24 (2014) 1674–1682, https://doi.org/10.1016/S1003-6326(14)63240-4.
[43] S. Kumar, P.S. Grant, K.A.Q. O'Reilly, Evolution of Fe bearing Intermetallics during DC casting and homogenization of an Al-Mg-Si Al alloy, Metall. Mater. Trans. A Phys. Metall. Mater. Sci. 47 (2016) 3000–3014, https://doi.org/10.1007/s11661-016-3451-5.
[44] G. Mrówka-Nowotnik, J. Sieniawski, M. Wierzbińska, Intermetallic phase particles in 6082 aluminium alloy, Arch. Mater. Sci. Eng. 28 (2007) 69–76.
[45] N.C.W. Kuijpers, F.J. Vermolen, C. Vuik, P.T.G. Koenis, K.E. Nilsen, S. van der Zwaag, The dependence of the β-AlFeSi to α-Al(FeMn)Si transformation kinetics in Al-Mg-Si alloys on the alloying elements, Mater. Sci. Eng. A 394 (2005) 9–19, https://doi.org/10.1016/j.msea.2004.09.073.
[46] J. Gonzalez, V. Lopez, A. Bautista, E. Otero, X.R. Nóvoa, Characterization of porous aluminium oxide films from ac impedance measurements, J. Appl. Electrochem. 2 (1999) 229–238, https://doi.org/10.1023/A:1003481418291.
[47] G. Boisier, A. Lamure, N. Pébère, N. Portail, M. Villatte, Corrosion protection of AA2024 sealed anodic layers using the hydrophobic properties of carboxylic acids, Surf. Coat. Technol. 203 (2009) 3420–3426, https://doi.org/10.1016/j.surfcoat.2009.05.008.
[48] V.R. Capelossi, M. Poelman, I. Recloux, R.P.B.B. Hernandez, H.G. De Melo, M. G. Olivier, Corrosion protection of clad 2024 aluminum alloy anodized in tartaric-sulfuric acid bath and protected with hybrid sol-gel coating, Electrochim. Acta 124 (2014) 69–70, https://doi.org/10.1016/j.electacta.2013.09.004.
[49] R. Figueroa, X.R. Nóvoa, C. Pérez, Hydrophobic surface treatments for improving the corrosion resistance of anodized AA2024-T3 alloys, Electrochim. Acta 303 (2019) 56–66, https://doi.org/10.1016/j.electacta.2019.02.034.
[50] J. Cabral-Miramontes, C. Gaona-Tiburcio, F. Estupinán-López, M. Lara-Banda, P. Zambrano-Robledo, D. Nieves-Mendoza, E. Maldonado-Bandala, J. Chacón-Nava, F. Almeraya-Calderón, Corrosion resistance of hard coat anodized AA 6061 in citric–sulfuric solutions, Coatings 10 (2020) 601, https://doi.org/10.3390/coatings10060601.
[51] J.R. MacDonald, Impedance Spectroscopy: Emphasizing Solid Materials and Systems, John Wiley & Sons, Inc., 1987.
[52] J. Hitzig, K. Jüttner, W.J. Lorenz, W. Paatsch, AC-impedance measurements on porous aluminium oxide films, Corros. Sci. 24 (1984) 945–952, https://doi.org/10.1016/0010-938X(84)90115-X.
[53] F.L. Zeng, Z.L. Wei, J.F. Li, C.X. Li, X. Tan, Z. Zhang, Z.Q. Zheng, Corrosion mechanism associated with Mg2Si and Si particles in Al-Mg-Si alloys, Trans. Nonferrous Met. Soc. China (English Ed) 21 (2011) 2559–2567, https://doi.org/10.1016/S1003-6326(11)61092-3.